Computer Assisted Methods in Engineering and Science
31(4): 487–506, 2024, doi: 10.24423/cames.2024.1697

Forecasting Phase-Field Variables in Brittle Fracture Problems by Autoregressive Integrated Moving Average Technique

Cuong T. NGUYEN1)*, Long H. LE2), Minh N. DINH3), Ngoc M. LA3)

1) *Center for Modeling, Simulation and Imaging in Medicine, Rensselaer Polytechnic Institute, 110 8th Street, Troy, NY 12180, USA*

2) *Automotive R&D Center, Bosch Vietnam, 33 Le Duan, Vietnam*

3) *School of Science, Engineering and Technology, RMIT University Vietnam, Ho Chi Minh City, Vietnam*

* *Corresponding Author e-mail: nguyec11@rpi.edu*

Phase-field modeling is a powerful and versatile computational approach for modeling the evolution of cracks in solids. However, phase-field modeling requires high computational cost for accurately capturing how cracks develop under increasing loads. In brittle fracture mechanics, crack initiation and propagation can be considered as a time series forecasting problem so they can be studied by observing changes in the phase-field variable, which represents the level of material damage. In this paper, we develop a rather simple approach utilizing the autoregressive integrated moving average (ARIMA) technique to predict variations of the phase-field variable in an isothermal, linear elastic and isotropic phase-field model for brittle materials. Time series data of the phase-field variable is extracted from numerical results using coarse finite-element meshes. Two ARIMA schemes are introduced to exploit the structure of the collected data and provide a prediction for changes in phase-field variable when using a finer mesh. This finer mesh gives a better results in terms of accuracy but requires significantly higher computational cost.

Keywords: fracture mechanics, brittle fracture, phase-field modelling, time-series forecasting.

1. INTRODUCTION

Fracture is one of the main failure modes in engineering materials and structures. Predicting the nucleation and propagation of cracks is, therefore, of great importance in engineering analysis and design. The theoretical foundations to understand brittle crack evolution were introduced and outlined in [1–3]. Following Griffith [1] and Irwin [2], crack propagation can be considered a stability problem, where if the energy release rate reaches a critical value, the crack starts to propagate. While Griffith's theory describes an adequate criterion for crack propagation, it is insufficient to determine curvilinear crack paths, crack kinking and branching.

Numerical approaches to fracture problems can be categorized into discontinuous crack and smeared crack models. In the former approach, cracks are represented as discrete entities with a discontinuous displacement field across the crack line (in 2D) or crack surface (in 3D). Representative methods in this approach include extended finite element methods (XFEM) [5] and remeshing strategies [6]. With these methods, however, the task of tracking crack paths can be challenging in problems with complex crack patterns, and their extension to complex three-dimensional problems is also nontrivial. Phase-field modeling (PFM) presented by [4] and [8] uses smeared crack models as an alternative. In this model, the discontinuity in the material is assumed to be not sharp, but instead is smeared over a localization band. This spatially diffuse fracture zone is coupled with an additional continuous field variable, which we refer to as the phase-field variable. Mathematically, PFM can be considered as a tool for solving fracture mechanics problems using partial differential equations (PDEs): it involves solving two PDEs, one for the vector displacement field and the other for the scalar phase-field variable. The advantage of PFM over FEM and XFEM is that PFM can handle complex crack shapes by changing the phase-field value on a fixed mesh. By doing so, there is no need to remesh when cracks propagate, like it is the case in FEM and XFEM. Therefore, the computational time and cost are greatly reduced without sacrificing accuracy. However, as PFM is still essentially a mesh-based method, so the mesh quality has a significant effect on the obtained results.

One of the main drawbacks of PFM is its high computational cost. Specifically, in order to accurately capture the crack phenomenon, a sufficiently refined mesh surrounding the crack tip is required. In this work we propose a rather simple approach based on a time-series forecasting technique in machine learning to address this issue by using the phase-field results from coarse meshes to predict the corresponding result from a finer mesh. In machine learning, in order to deal with time-dependent variables there are two main approaches: statistical methods and artificial neural networks. Given a time series, Holt–Winters, [9] forecasting models the three exponentially weighted moving average (EWMA) aspects including the average value, the trend over time, and the seasonality. The model makes predictions by computing the combined effects of these three factors. On the other hand, the autoregressive integrated moving average (ARIMA) framework [10] models how each data point in the time series is influenced by its previous values (autoregressive), and integrates this knowledge with a moving average part, which computes the linear combination of several data points, to make predictions. As a result, Holt–Winters works better for seasonal time series while ARIMA works better for non-stationary time series. In this paper, PFM is used to build a model for brittle fracture problems based on the theoretical fracture model of Griffith. The results of PFM for the coarse mesh of brittle fracture plate with three successively coarse meshes are used as a database. Then, ARIMA is employed to forecast the outcomes for the finer mesh as the finite-element meshes are refined. Next, the predicted results are compared with the true data obtained using PFM with the actual discretization in the finer mesh.

The paper is structured as follows. Section 2 is dedicated to the overview of the phase-field framework for brittle fracture problems. Additionally, a series of representative numerical examples is also examined for the purpose of generating data and and verifying our predictions. In Subsec. 3.1 we present a brief review of ARIMA as a time-series forecasting technique. Our main contributions are presented in Subsec. 3.2, in which we propose two ARIMA schemes for predicting the phase-field variable. The accuracy and efficiency of the two proposed schemes are illustrated in Sec. 4. Finally, Sec. 5 concludes the paper by summarising key findings and discussing their implications.

2. PHASE-FIELD MODELING OF BRITTLE FRACTURE

We begin by reviewing the theoretical foundations of brittle fracture mechanics and the phase-field modeling approach. Then, in Subsec. 2.5, we present a series of numerical examples covering both two-dimensional and three-dimensional brittle fracture problems.

2.1. Griffith's theory and the variational approach

The theory of linear elastic fracture mechanics was first introduced in 1920 by Griffith [1]. In his approach, the competition between the bulk energy away from the crack and the surface energy on the crack results in crack propagation. The stress intensity factor approach introduced in [2] focuses on the stress state around the crack tip and is also a useful method in engineering practice.

We consider a body occupying the domain $\Omega \subset \mathbb{R}^n$ with spatial dimension $n \in \{2, 3\}$, where a crack set $\Gamma \subset \mathbb{R}^{n-1}$ is included. Under this problem setting, the total energy functional is given by:

$$\mathcal{E} := \Psi_s - \mathcal{W} + \Psi_c, \tag{1}$$

where the stored strain energy Ψ_s, the external work $\mathcal{W}$, and the surface energy Ψ_c are defined as:

$$\Psi_s(\mathbf{u}) = \int\limits_{\Omega\backslash\Gamma} \psi(\boldsymbol{\epsilon}(\mathbf{u}), \Gamma) dV, \qquad \mathcal{W} = \int\limits_{\Omega} \mathbf{b}^* \cdot \mathbf{u} dV + \int\limits_{\partial\Omega_t} \mathbf{t}^* \cdot \mathbf{u} dA,$$
$$\Psi_c(\Gamma) = \int\limits_{\Gamma} g_c dA, \tag{2}$$

where g_c is the critical energy release rate or fracture toughness, and $\mathbf{b}^*$ and $\mathbf{t}^*$ are the body force and traction, respectively. The global minimizer of the total energy functional $\mathcal{E}$ leads to the solution of the problem under consideration:

$$(\mathbf{u}(t), \Gamma(t)) = \arg\{\min \mathcal{E}(\mathbf{u}, t)\}. \tag{3}$$

This problem is essentially a moving boundary value problem since Γ changes over time. In order to overcome the difficulty associated with the moving boundary, the surface integral is replaced by a volume integral as follows [7]:

$$\Psi_c = \int\limits_{\Gamma} g_c dA \approx \int\limits_{\Omega} g_c \gamma dV, \tag{4}$$

where γ is the the crack density, which depends on a length-scale parameter l_c and the continuous scalar-valued phased-field ϕ. These quantities will be discussed in detail in the subsequent sections.

2.2. Phase-field approximation with a diffusive crack topology

For quasi-static brittle fracture in isotropic elastic solids, cracks are approximated as finite bands characterized by a crack phase-field variable ϕ: $\phi = 1$ denotes fully broken material and $\phi = 0$ represents intact one. To illustrate the idea behind the concept of a diffuse crack topology, it is ideal to consider an infinite bar with cross-section A aligned along the x-axis [8]. The domain under consideration is $\mathcal{B} = A \times L$, where $L = (-\infty, +\infty)$ and position $x \in L$. A fully opened crack is specified at $x = 0$. The sharp crack profile can be described by the phase-field variable $\phi(x) \in [0, 1]$ defined as follows:

$$\phi(x) := \begin{cases} 1 & \text{for } \; x = 0, \\ 0 & \text{otherwise.} \end{cases} \tag{5}$$

Following the physical observation that a crack itself initiates with micro-cracks and nano-voids, it is essentially not a discrete phenomenon. Therefore, the non-smooth phase-field is replaced by a smeared counterpart, defined by the following exponential function:

$$\phi(x) = e^{-|x|/l_c}, \tag{6}$$

where l_c is the length-scale parameter. We observe that $\phi(x) = e^{-|x|/l_c}$ is the solution of the homogeneous second-order differential equation:

$$\phi(x) - l_c^2 \phi''(x) = 0. \tag{7}$$

This is subject to Dirichlet boundary conditions $\phi(0) = 1$, $\phi(\pm\infty) = 0$, with the solution to the associated characteristic equation $1 - l_c^2 s^2 = 0$ given by $s = \pm 1/l_c$. The corresponding variational of this Euler equation can be written as:

$$\phi = \arg\left\{ \inf_{\phi \in W} I(\phi) \right\}, \quad \text{where} \quad I(\phi) = \frac{1}{2} \int\limits_{\mathcal{B}} (\phi^2 + l_c^2 \phi'^2) dV, \tag{8}$$

and $W = \{\phi | \phi(0) = 1,\ \phi(\pm\infty) = 0\}$. Substituting $dV = Adx$ into the expression for the functional $I(\phi)$ leads to $I(\phi = e^{-|x|/l_c}) = l_c A$. Then, we define the fracture surface density as:

$$\begin{aligned} \Gamma(\phi) &= \frac{I(\phi)}{l_c} = \frac{1}{2l_c} \int\limits_{\mathcal{B}} (\phi^2 + l_c^2 \phi'^2) dV = \int\limits_{\mathcal{B}} \gamma(\phi, \phi') dV, \\ \gamma(\phi, \phi') &= \frac{1}{2l_c} \phi^2 + \frac{l_c}{2} \phi'^2. \end{aligned} \tag{9}$$

2.3. Strain energy degradation

The formulation for cracks in multi-dimensional solids can be obtained in a straightforward manner by extending the formula for one-dimensional solids presented in the preceding section. Specifically, replacing the ordinary derivative ϕ' with the gradient $\nabla\phi$ leads to the crack surface density function per unit volume for a multi-dimensional solid:

$$\gamma(\phi, \phi') \to \gamma(\phi, \nabla\phi) = \frac{1}{2l_c} \phi^2 + \frac{l_c}{2} \nabla\phi^2.$$

Then, the surface energy Ψ_c is approximated as:

$$\Psi_c = \int\limits_{\Gamma} g_c d\Gamma \approx \int\limits_{\Omega} g_c \gamma(\phi, \nabla\phi) dV,$$

where the sharp crack surface is regularized by the functional

$$\Gamma \approx \Gamma_l(\phi) = \int\limits_{\Omega} \gamma(\phi, \nabla\phi) dV.$$

Due to the damage caused by cracks, the strain energy density is degraded by the function $g(\phi)$:

$$\psi(\boldsymbol{\epsilon}, \phi) = g(\phi)\psi_0(\boldsymbol{\epsilon}),$$

where $g(\phi)$ is the degradation function and $\psi_0(\boldsymbol{\epsilon})$ is the initial free energy density function. There are many choices for the function $g(\phi)$, but we choose the most basic one $g(\phi) = (1-\phi)^2 + \kappa$ introduced in [7], in which κ is a small number responsible for keeping the system of equations stable. Then, the total internal energy can be approximated as:

$$\Psi = \Psi_s + \Psi_c \approx \int\limits_{\Omega} \left[((1-\phi)^2 + \kappa)\psi_0(\boldsymbol{\epsilon}) + g_c\gamma(\phi, \nabla\phi)\right] dV,$$

we introduce a so-called history variable $H = \max(\psi_0(\boldsymbol{\epsilon}), H_n)$, where H_n is the computed energy history at the previous step n [11]. This enforces the irreversibility of the damage $\dot{\phi} \geq 0$, which leads to the Karush–Kuhn–Tucker conditions [12]:

$$\dot{H} \geq 0, \quad \psi_0 - H \leq 0, \quad \dot{H}(\psi_0 - H) = 0. \tag{10}$$

2.4. Finite element implementation

Within the finite-element framework, the displacement $\mathbf{u}$ and the phase-field variable ϕ are discretized using the standard Galerkin method [15] as follows:

$$u_i^h = \sum_{A=1}^{n_b} N^A u_i^A, \qquad \phi^h = \sum_{A=1}^{n_b} N^A \phi^A, \tag{11}$$

where n_b is the dimension of the discrete space, N^A are the basis functions, and u_i^A and ϕ^A are the nodal degrees-of-freedom for the displacement and phase-field. Taking the variation of two energies ($\delta\Psi = \delta\Pi^u = 0$, where $\Pi^u = \Psi - \mathcal{W}$) and adopting a staggered solution scheme, we arrive at a combined system of equations:

$$\begin{cases} \phi_{n+1} = \arg\left\{\inf\limits_{\phi} \int\limits_{\Omega} \left[g_c\gamma\left(\phi, \nabla\phi\right) + (1-\phi)^2 H\right] dV\right\} \rightarrow \mathbf{K}_n^{\phi}\phi_{n+1} = -\mathbf{r}_n^{\phi}, \\ \mathbf{u}_{n+1} = \arg\left\{\inf\limits_{u} \int\limits_{\Omega} \left[\psi\left(\mathbf{u}, \phi_n\right) - \mathbf{b}^* \cdot \mathbf{u}\right] dV - \int\limits_{\partial\Omega} \mathbf{t}^* \cdot \mathbf{u} dA\right\} \rightarrow \mathbf{K}_n^u \mathbf{u}_{n+1} = -\mathbf{r}_n^u, \end{cases} \tag{12}$$

where the tangent stiffness matrices for the displacement and phase-field solutions are computed as:

$$\begin{cases} \mathbf{K}_n^u = \int\limits_{\Omega} \left\{ \left[(1-\phi_n)^2 + \kappa \right] \mathbf{B}^T \mathbf{C}_0 \mathbf{B} \right\} dV, \\ \mathbf{K}_n^{\phi} = \int\limits_{\Omega} \left\{ \left[g_c/l_c + 2H \right] \mathbf{N}^T \mathbf{N} + g_c l_c \mathbf{B}^T \mathbf{B} \right\} dV, \end{cases} \tag{13}$$

and the residuals are given by:

$$\begin{cases} \mathbf{r}_n^u = \mathbf{f}_{\text{int}} - \mathbf{f}_{\text{ext}} = \int\limits_{\Omega} \left[(1-\phi_n)^2 + \kappa \right] \boldsymbol{\sigma} \mathbf{B} d\Omega - \int\limits_{\Omega} \mathbf{b}^* \cdot \mathbf{N}^T dV - \int\limits_{\partial\Omega_t} \mathbf{t}^* \cdot \mathbf{N}^T dA, \\ \mathbf{r}_n^{\phi} = \int\limits_{\Omega} \left\{ \left[g_c \phi_n / l_c - 2(1-\phi_n) H \right] \mathbf{N}^T + g_c l_c \mathbf{B}^T \nabla \phi_n \right\} dV, \end{cases} \tag{14}$$

where $\mathbf{N} = [N^A]$, $A = 1, 2, ..., n_b$ is the row vector of shape functions and $\mathbf{B}$ is the gradient of the shape function matrix. Equation (12) can be rewritten in a compact form, which is more convenient in implementation:

$$\begin{bmatrix} \mathbf{K}_n^u & 0 \\ 0 & \mathbf{K}_n^{\phi} \end{bmatrix} \begin{bmatrix} \mathbf{u}_{n+1} \\ \phi_{n+1} \end{bmatrix} = - \begin{bmatrix} \mathbf{r}_n^u \\ \mathbf{r}_n^{\phi} \end{bmatrix}. \tag{15}$$

2.5. Representative numerical examples

In this subsection, we present several numerical examples in which phase-field data is generated by using the phase-field model for the purpose of training and testing our machine learning algorithms. We first start with a benchmark test of a single element in plane-strain. Then, numerical experiments for a single edge-notched plate in tension, shear and mixed modes are carried out to obtain the phase-field time series at the crack tip. A tensile test of a plate with two symmetrically arranged notches is also studied. Finally, we examine a three-dimensional problem under tensile loading.

2.5.1. Benchmark test. In order to verify the numerical results produced by our phase-field modeling, we consider a two-dimensional element in plane strain, depicted in Fig. 1. Table 1 summarizes the geometric dimensions and material properties. The bottom nodes are constrained in both directions while the top nodes are free to slide vertically. A prescribed displacement v is applied in 1000 steps, with an increment of $\Delta v = 10^{-4}$ mm per step. This example

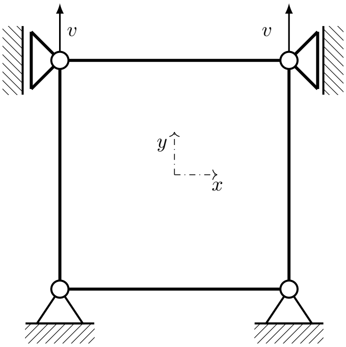

FIG. 1. One-element problem.

TABLE 1. Parameters used in one-element problem.

Dimensions [mm × mm]	Young's modulus [kN/mm^2]	Poisson's ratio	Critical energy release rate [kN/mm]	Length scale [mm]
1×1	$E = 210$	$\nu = 0.3$	$g_c = 5 \times 10^{-3}$	$l_c = 0.1$

is served as a benchmark test, as its analytical solution exists, so we are able to verify our numerical results. The exact solution describing the relationship between the phase-field and vertical strain is given by [11]:

$$\phi(\varepsilon_y) = \frac{\varepsilon_y^2 l_c c_{22}}{g_c + \varepsilon_y^2 l_c c_{22}}, \tag{16}$$

where c_{22} is the entry in row 2 and column 2 of the stiffness matrix $\mathbf{C}_0$, and it can be computed as:

$$c_{22} = \frac{E(1-\nu)}{(1+\nu)(1-2\nu)}. \tag{17}$$

Once the exact phase-field $\phi(\varepsilon_y)$ is determined, the vertical stress is related to the phase-field as:

$$\sigma_y = c_{22}\varepsilon_y \left[1 - \phi(\varepsilon_y)\right]^2. \tag{18}$$

The variations of phase-field variable and stress as a function of the vertical strain are plotted in Fig. 2. As can be seen from this figure, the numerical solution obtained from phase-field modeling matches very well with the analytical one.

2.5.2. Single-edge notched and symmetric double-notched tensile tests. Next, we consider the well-known single-edge notched tension test. The geometry and the boundary conditions of a squared plate are depicted in Fig. 3 (left).

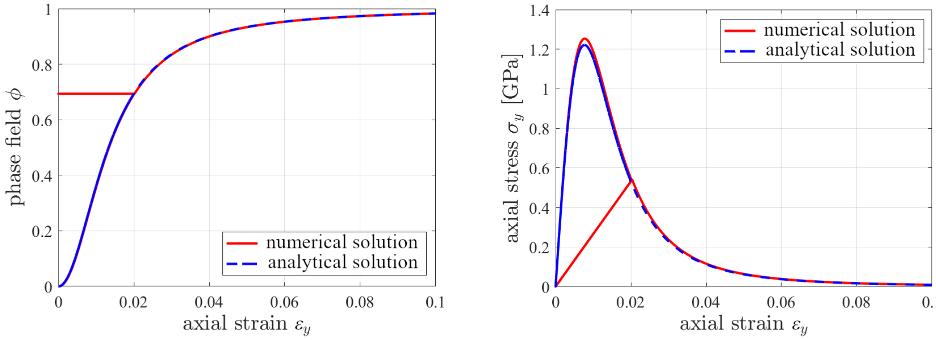

FIG. 2. One-element problem: phase-field ϕ (left) and axial stress σ_y (right) versus axial strain ε_y.

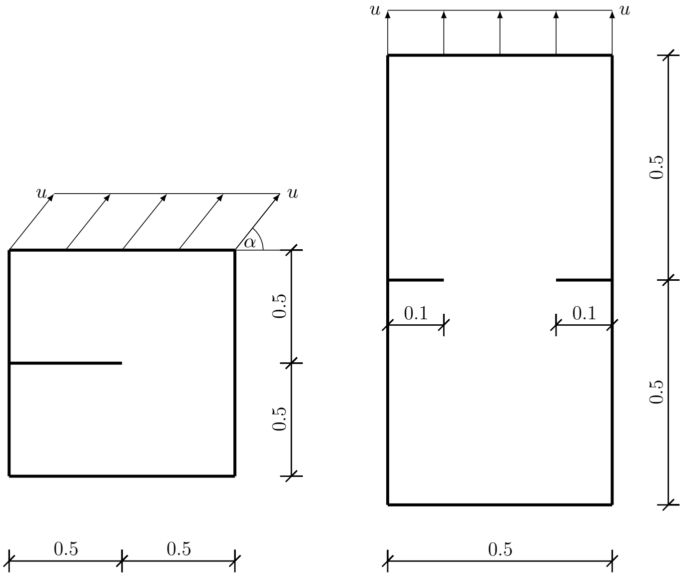

FIG. 3. Two-dimensional problems: single-edge notched specimen (left) and double-notched specimen (right).

There is an initial notch in the horizontal direction, at middle height from the left edge of the plate to its center. Material parameters are specified similarly to those in the one-element example (Subsec. 2.5.1), except that $g_c = 2.7 \times 10^{-3}$ kN/mm and the length scale is chosen as $l_c = 4h$, where h is the element size. The loading is applied with $\Delta u = 5 \times 10^{-5}$ mm.

In this example, the specimen is discretized with four finite element mesh sizes to gradually increase number of elements: 1600 (40×40), 2500 (50×50), 3600 (60×60) and 4900 (70×70). We examine three cases representing three typical failure modes in two-dimensional fracture problems: $\alpha = 90°$ (mode I – tension), $\alpha = 0$ (mode II – pure shear), and $\alpha = 45°$ (mixed mode). The evolution of the phase-field variable at the crack tip in these problems is plotted in Fig. 4. In the symmetric double-notched tensile test shown in Fig. 3 (right), the length of the vertical side of the specimen is twice that of the horizontal one. So, four meshes are specified as 40×80, 50×100, 60×120 and 70×140. The displacement-controlled loading is applied in $N = 200$ steps with an increment $\Delta v = 10^{-4}$ mm.

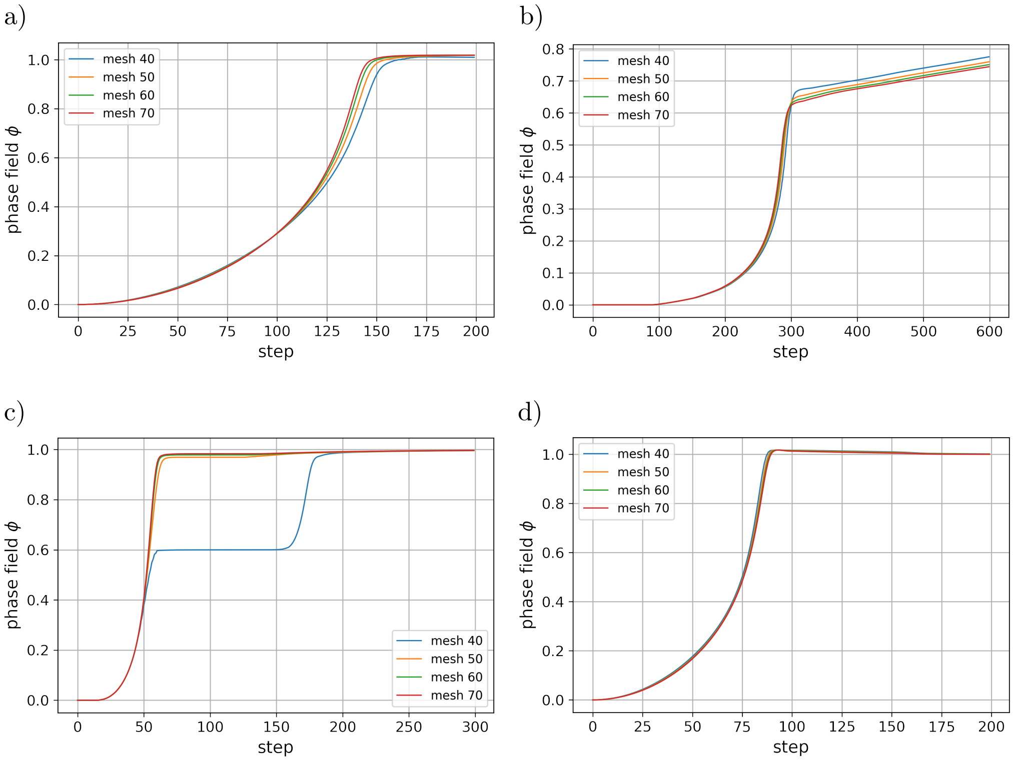

FIG. 4. Variations of the phase-field variable in two-dimensional problems: single-edge notched: a) $\alpha = 90°$, b) $\alpha = 0°$, c) $\alpha = 45°$; d) symmetric doubled-notched.

As can be seen in Fig. 4, there are clear trends of the phase-field values in the four mesh sizes of these problems. Specifically, the value of phase-field variable changes and tends to converge when refining the mesh. In principle, the results will be more accurate when increasing the mesh size. However, refining the mesh leads to a significant increase in the computational cost. Instead of using a finer mesh, we predict the variation of the phase-field variable using time-series modeling techniques, which will be discussed in detail in Subsec. 3.2. The goal is to utilize coarse-grain crack propagation data and train ARIMA models to predict the results of the finest mesh.

2.5.3. Three-dimensional single notched test. We consider the three-dimensional tensile test specimen depicted in Fig. 5. The bottom face is constrained and the top face is subject to a uniformly prescribed displacement $\Delta u = 10^{-3}$ mm for $N = 1000$ steps. The material properties and geometric dimensions are chosen according to [8], as summarized in Table 2. The variations of the phase-field variable in this 3D problem are shown in Fig. 6.

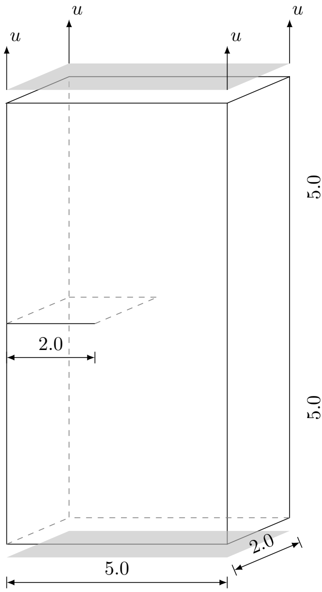

Fig. 5. Three-dimensional single-notched test.

Table 2. Parameters used in the three dimensional single notched test.

Dimensions [mm × mm × mm]	Young's modulus [kN/mm^2]	Poisson's ratio	Critical energy release rate [kN/mm]	Length scale
$5 \times 10 \times 2$	$E = 20.8$	$\nu = 0.3$	$g_c = 5 \times 10^{-4}$	$l_c = 4h$

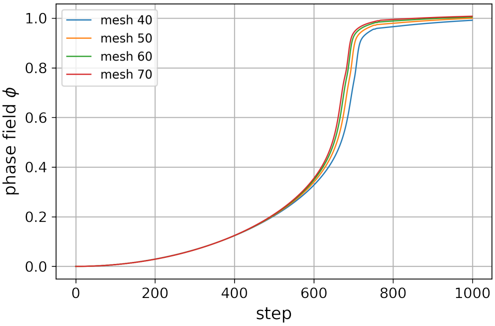

Fig. 6. Variations of the phase-field variable in the three-dimensional problem.

3. ARIMA

This section presents our proposed training algorithms implementing the ARIMA technique. We start with a brief review of ARIMA as a time series forecasting method in Subsec. 3.1. Then, we introduce two approaches to training using ARIMA to predict the phase-field variable in Subsec. 3.2. The phase-field value changes and tends to converge as the mesh size increases, becoming more accurate with smaller element lengths. We investigate how crack propagation can be predicted using time series modeling techniques.

3.1. ARIMA as a time series forecasting

A time-series consists of past observations that can be mined to discover internal structures such as autocorrelation, trend, and seasonal variation. Furthermore, these insights can be used to deliver monitoring and prediction capacities. If we consider a time series with past observations as a discrete variable where X_t denotes the observation at time t, and ϵ_t denotes the zero-mean random noise term at time t, with discrete time steps at an interval Δt, we establish an autoregression (AR) model such as:

$$X_t = \sum_{i=1}^{k} \alpha_i X_{t-i\Delta t} + \epsilon_t. \tag{19}$$

Then, the noise term is presented using a moving average (MA) model such as:

$$X_t = \sum_{i=1}^{q} \beta_i \epsilon_{t-i\Delta t} + \epsilon_t. \tag{20}$$

To fit the best model for the time-series with independent noise terms, the autoregressive moving average (ARMA) framework [14] integrates the linear function of previous time steps with the independent random noise minus a fraction of the previous random noise. The ARMA model takes two parameters (k, q):

- k – the "autoregressive" term: represents the lags of the series in the prediction process;
- q – the "moving average" term: represents the lags of the forecast errors.

Nonetheless, ARMA cannot be used effectively for non-stationary time series. To address this drawback, the autoregressive integrated moving average (ARIMA) framework, an extension of ARMA, integrates the differencing of past observations (at consecutive time steps) to "stationarize" the time series before applying the standard ARMA scheme [10]. As a result, the ARIMA framework includes the parameter d, capturing the differencing level. The complete ARIMA scheme is described as follows.

A random variable is considered a stationary time series if its statistical properties such as first and second moments remain approximately constant over time. Visualizing a stationary series shows that the data points vary around its mean with relatively constant amplitude. The ARIMA framework, an extension of ARMA, addresses this limitation by integrating the differencing of raw observations to allow the time series to become stationary [10]. Accordingly, the ARIMA framework introduces an extra parameter d, and performs time series forecasting for nonstationary series as follows:

$$\begin{aligned} \nabla^d X_t &= \epsilon_t + \sum_{i=1}^{k} \alpha_i \nabla^d X_{t-i} + \sum_{i=1}^{q} \beta_i \epsilon_{t-i}, \\ \widetilde{X}_t &= \nabla^d \widetilde{X}_t + \sum_{i=1}^{d-1} \nabla^i X_{t-i}. \end{aligned} \tag{21}$$

To conclude, an ARIMA (k, d, q) forecasting model not only performs the "signal filtering" act but also the "trend filtering" act by applying the d^{th}-order differencing, inducing past observations into future forecasts.

Considering our brittle fracture analysis process as a time series, we need to determine the parameters (k, d, q) to construct an ARIMA forecasting model. First, because computational simulations such as the isotropic brittle fracture model do not generate noise, we argue that q can be set to zero. Second, as the original time series is not stationary, we need to conduct a stationary study to determine the appropriate order of differencing for our time series. We discuss how to identify suitable values for parameters d and k below:

- k: the number of autoregressive terms (i.e., the lagged value),
- d: the number of differences needed to achieve stationarity,
- q: the noise term.

3.1.1. Order of differencing d. A stationary time series means no differencing is needed, thus $d = 0$. Our study shows that our time series is nonstationary and the order of differencing (essential for our ARIMA model) can be computed as follows, where Δd denotes the d^{th} difference of time series X; we define the following differencing levels:

$$d = 1 : \Delta_t^1 = X_t - X_{t-1}, \tag{22}$$

$$d = 2 : \Delta_t^2 = (X_t - X_{t-1})(X_{t-1} - X_{t-2}). \tag{23}$$

Referring to [13], we detect a constant increasing/decreasing trend in our original time series. Further study shows that one order of differencing (i.e., $d = 1$) stationarizes our target time series so that the ARMA process can be conducted to perform forecasting of the phase-field values over time.

3.1.2. Number of autoregressive terms k. Our time-series analysis framework handles sequential observations at every time-step and updates the forecasting buffer simultaneously. This is a conventional approach for many time-step-based applications, and $k = 1$ (i.e., AR(1)) is applicable to our ARIMA model.

As a result, we study an initial ARIMA(1,1,0) model which can be described as "the differenced first-order auto-regressive model". To conclude, this ARIMA model regresses the first difference of a collection of observable phase-field values as a non-stationary time series, with the lag value of one period.

3.2. ARIMA for phase-field forecasting

As can be seen in Subsec. 2.5, the change of the phase-field variable versus the prescribed displacement step can be considered as time-series data. Therefore, ARIMA is a promising candidate, that can be used to train the collected data from coarse meshes and provide a prediction for the results of finer mesh. In this section, we present two training ways using ARIMA for predicting phase-field variable for the problems presented in the preceding section. The numerical results obtained using the finest mesh in each example are considered the most accurate among the given four mesh grids. Our objective is to use the results from three coarser meshes, e.g. 40×40, 50×50 and 60×60 to predict the results of the 70×70 mesh in the single-edge notched test example.

3.2.1. Out-of-time training (ARIMA1). The data of the phase-field variable at the crack tip for various mesh sizes are collected and divided into two folds: training and testing. In this model, we use the complete result of a base mesh, which can be mesh 40, mesh 50, or mesh 60 and a portion $R\%$ of mesh 70 to predict its own remaining part, i.e., $(100 - R)\%$. After being trained using full data of the base mesh and the training part of the finer mesh, the remaining part of the fine mesh will be predicted. Figure 7 describes the process of training in detail.

3.2.2. Across-grids training (ARIMA2). The advantage of out-of-time forecasting ARIMA presented in Subsec. 3.2.1 is that the accuracy can be improved proportionally with the size $R\%$ of the training data. However, in many cases, the partitioned data of the highly accurate results (mesh 70) does not exist. In addition, the accuracy of ARIMA1 is limited since the trend is strongly affected by the chosen base mesh. Therefore, ARIMA2 is introduced to overcome these weaknesses. In particular, in ARIMA2, we use the full data of the three coarse meshes, which can be easily achieved as the database to predict the fine mesh solution. We consider the phase-field variable across meshes at each step

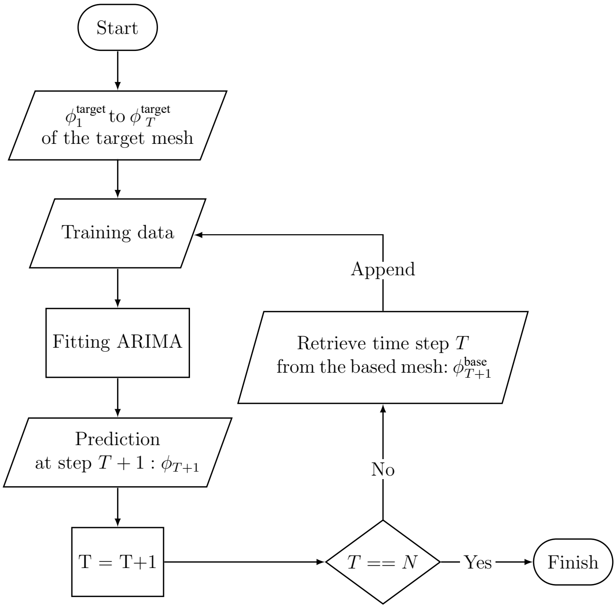

Fig. 7. ARIMA1: Out-of-time training process.

as a short-time time series. It is clear that it has a trend converging to the exact solution when the mesh gets finer. We assume that the phase-field prediction in the next finer mesh at the same loading step can be represented as a linear function of the difference in phase-field values and residual errors at coarser meshes. At each step, we go across mesh size grids, and we train an ARIMA model based on the corresponding results of meshes 40, 50 and 60, then produce a prediction for the mesh 70. It is clear that with this training method we are predicting a short-time series, so it is better to update the order of the moving-average model $q = 1$. The detailed training process is illustrated in Fig. 8.

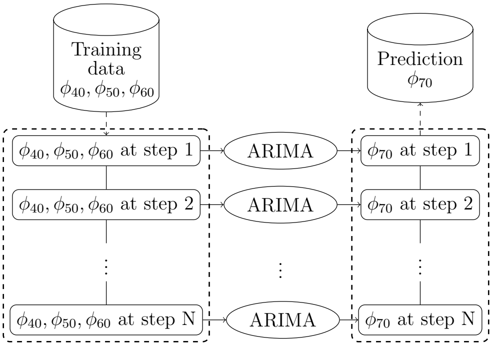

Fig. 8. ARIMA2: Across-grids training process.

3.2.3. Performance assessment metric. In assessing the accuracy of predictions obtained by forecasting models the root-mean-square error (RMSE) is frequently used. It measures the difference between the predicted values and the ground truth in L_2 norm and is defined as follows:

$$\mathrm{RMSE} = \sqrt{\frac{1}{N}\sum_{i=1}^{N}(x_i - \widehat{x}_i)^2}, \tag{24}$$

where N is the total number of observations, x_i is the actual value and $\widehat{x}_i$ is the predicted one. The reason for using RMSE is that it penalizes large errors, thus helping to rank the performance of forecasting techniques.

4. PREDICTIVE RESULTS

4.1. Training and predicting the phase-field variable

As shown in Table 3, the errors when using ARIMA1 decrease as the based mesh is chosen closer to the predictive mesh. The more true data we use (the higher value of R), the more accurate the results is observed. Figure 9 shows the prediction of the phase-field for mesh 70 with a training set $R = 60\%$ and

TABLE 3. RMSE results of two ARIMA approaches.

Problem	ARIMA1 (Phase-field ϕ)				ARIMA2	
	Base	30%	40%	50%	Phase-field ϕ	Reaction force
Tension $\alpha = 90°$	Mesh 40	0.044941	0.044861	0.044815	0.001555	0.003952
	Mesh 50	0.023772	0.023730	0.023647		
	Mesh 60	0.009785	0.009726	0.009733		
Pure shear $\alpha = 0°$	Mesh 40	0.028423	0.028114	0.021058	0.001943	0.002317
	Mesh 50	0.014916	0.014544	0.010444		
	Mesh 60	0.006528	0.006635	0.004422		
Mixed-mode $\alpha = 45°$	Mesh 40	0.199574	0.158567	0.102213	0.003474	0.007625
	Mesh 50	0.005951	0.004003	0.001696		
	Mesh 60	0.002123	0.001524	0.000766		
Double-notch	Mesh 40×80	0.015644	0.009836	0.003424	0.002657	0.005326
	Mesh 50×100	0.009256	0.006699	0.003424		
	Mesh 60×120	0.005150	0.0047960	0.003412		
	Base	40%	50%	60%	Phase-field ϕ	
3D problem	Mesh 40×80×4	0.050916	0.050090	0.050228	0.004952	
	Mesh 50×100×4	0.026872	0.026759	0.026084		
	Mesh 60×120×4	0.012637	0.011345	0.010743		

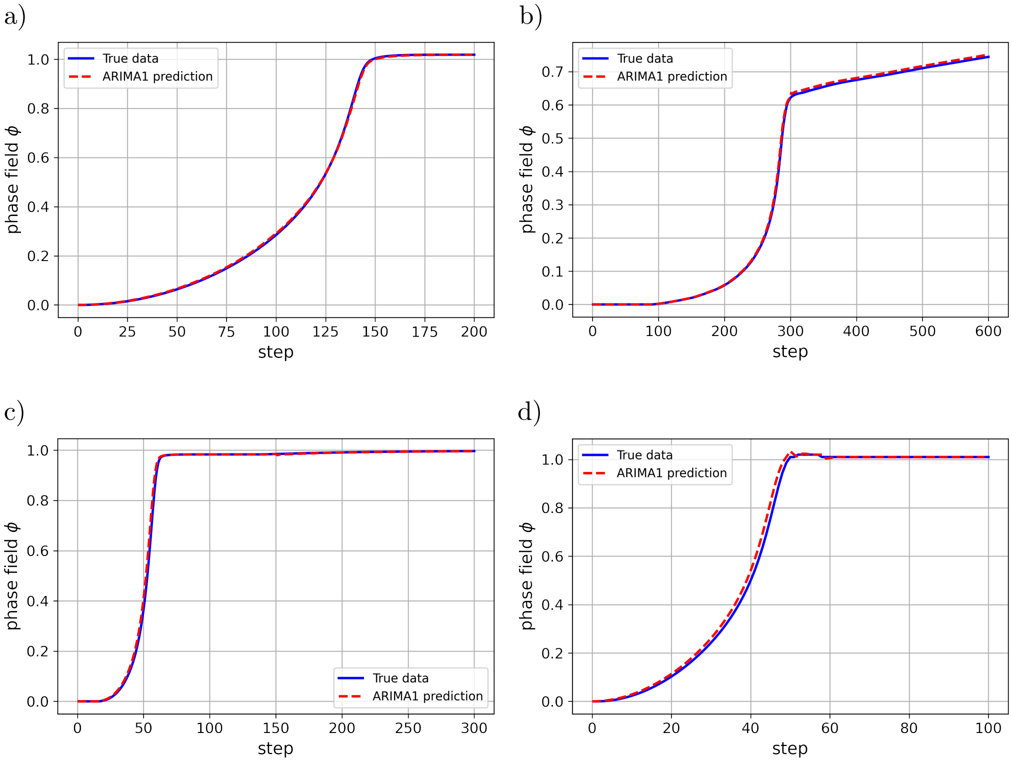

Fig. 9. Training results using ARIMA1:
single-edge notched: a) $\alpha = 90°$, b) $\alpha = 0°$, c) $\alpha = 45°$; d) symmetric doubled-notched.

the based mesh being 60. The prediction matches fairly well with the ground data obtained from running the mesh 70. Figure 10 presents the training results when $\alpha = 0°$ (shear mode) using ARIMA2, illustrating the model's accuracy in predicting phase-field variables under shear conditions The more true data we use (the higher value of R), the more accurate the results become. As shown

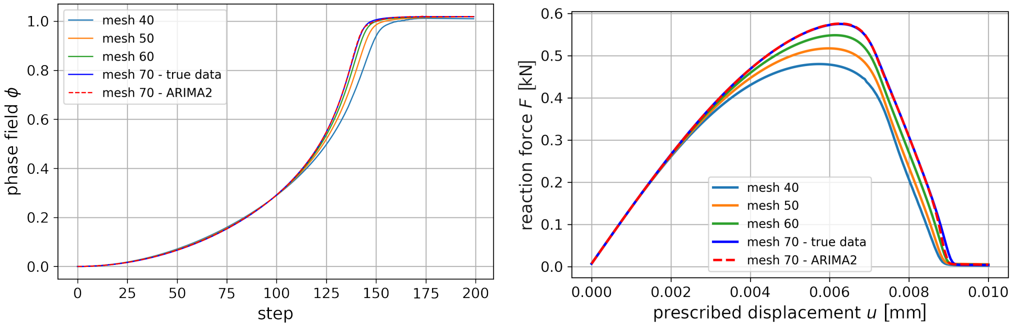

Fig. 10. Training results using ARIMA2 when $\alpha = 90°$ (tension).

in Fig. 11, the ARIMA2 training results for $\alpha = 90°$ (tension mode) closely align with the ground truth data, underscoring the method's reliability in tension scenarios. Overall, we can see that ARIMA2 gives a better agreement in comparison to ARIMA1. The improvement in accuracy can be explained by the data structures in the two training algorithms. Figure 12 presents the training results for the mixed-mode problem ($\alpha = 45°$) using ARIMA2. The figure highlights the strong agreement between the predictions and the ground truth data, demonstrating the robustness of ARIMA2 for capturing complex crack propagation trends in mixed-mode scenarios. The double-notch tension test results in Fig. 13 confirm that ARIMA2 accurately predicts phase-field variables across the notched regions, even under symmetric load conditions. In ARIMA2, the training data is structured as short-term data series, which can benefit from ARIMA model's capabilities. In short, the ARIMA2 model with the across-grids approach gives better results in most cases, without using any part of the finest mesh data. Figure 14 illustrates the training and prediction results for the three-dimensional problem using the ARIMA2 scheme. The figure demonstrates the improved accuracy and convergence of predictions compared to the true data, further validating the effectiveness of ARIMA2 in modeling phase-field variables across complex three-dimensional scenarios.

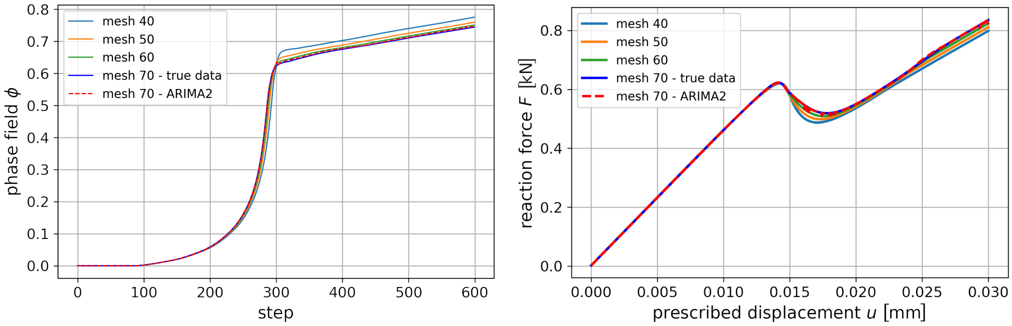

FIG. 11. Training results using ARIMA2 when $\alpha = 0°$ (shear).

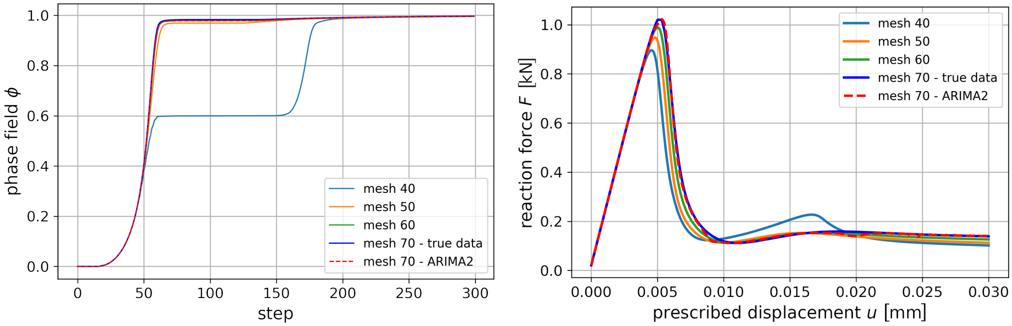

FIG. 12. Training results using ARIMA2 when $\alpha = 45°$ (mixed-mode).

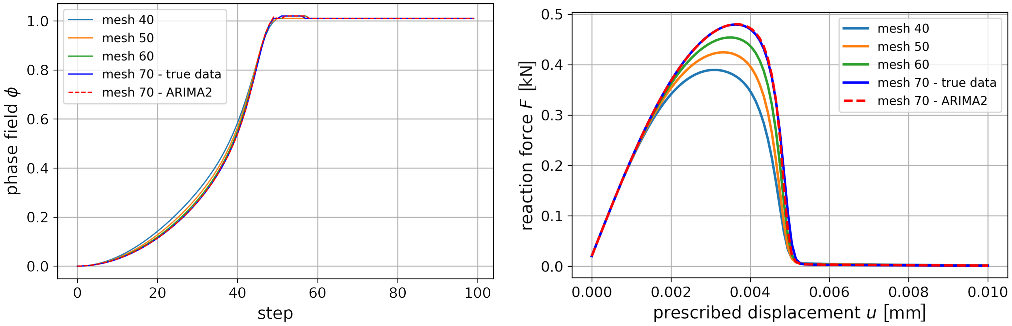

Fig. 13. Training results using ARIMA2 for the double-notch problem.

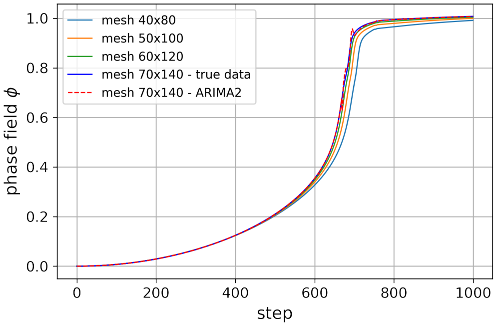

Fig. 14. Training results using ARIMA2 for the three-dimensional problem.

4.2. Training and predicting the reaction force by ARIMA2

When comparing the two ARIMA schemes for predicting the phase-field variable, we observed that ARIMA2 performs outstandingly. Therefore, we proceed to investigate its ability to predict the reaction force. It turns out that ARIMA2 also performs very well in this predictive task. As we can see in Table 3, the RMSE when using ARIMA2 is always less than 0.008.

5. CONCLUSION

In this study, the time series approach based on ARIMA models was utilized to train and predict the numerical results obtained by using phase-field modeling for brittle fracture problems. Numerical examples ranging from two-dimensional to three-dimensional problems were presented to show the performance of the two proposed ARIMA schemes in predicting the phase-field variable. The results show that it is feasible to use data from coarse meshes to predict the value of the phase-field variable in a denser mesh, especially with the ARIMA2 scheme. The application of ARIMA2 is also valid for predicting the reaction force.

REFERENCES

1. A.A. Griffith, The phenomena of rupture and flow in solids, *Philosophical Transactions of the Royal Society A: Mathematical, Physical and Engineering Sciences*, **221**(582–593): 163–198, 1921, doi: 10.1098/rsta.1921.0006.
2. G.R. Irwin, Fracture, [in:] *Elasticity and Plasticity*, Springer, Berlin, pp. 551–590, 1958.
3. G.I. Barenblatt, The mathematical theory of equilibrium cracks in brittle fracture, *Advances in Applied Mechanics*, **7**: 55–129, 1962, doi: 10.1016/S0065-2156(08)70121-2.
4. G.A. Francfort, J.J. Marigo, Revisiting brittle fracture as an energy minimization problem, *Journal of the Mechanics and Physics of Solids*, **46**(8): 1319–1342, 1998, doi: 10.1016/S0022-5096(98)00034-9.
5. N. Moës, J. Dolbow, T. Belytschko, A finite element method for crack growth without remeshing, *International Journal for Numerical Methods in Engineering*, **46**: 131–150, 1999, doi: 10.1002/(SICI)1097-0207(19990910)46:1<131::AID-NME726>3.0.CO;2-J.
6. R. Branco, F.V. Antunes, J.D. Costa, A review on 3D-FE adaptive remeshing techniques for crack growth modelling, *Engineering Fracture Mechanics*, **141**: 170–195, 2015, doi: 10.1016/j.engfracmech.2015.05.023.
7. B. Bourdin, G.A. Francfort, J.J. Marigo, The variational approach to fracture, *Journal of Elasticity*, **91**: 5–148, 2008, doi: 10.1007/s10659-007-9107-3.
8. C. Miehe, F. Welschinger, M. Hofacker, Thermodynamically consistent phase-field models of fracture: Variational principles and multi-field FE implementations *International Journal for Numerical Methods in Engineering*, **83**: 1273–1311, 2010, doi: 10.1002/nme.2861.
9. E.S. Gardner Jr., Exponential smoothing: The state of the art, *Journal of Forecasting*, **4**(1): 1–28, 1985, doi: 10.1002/for.3980040103.
10. P.J. Brockwell, R.A. Davis, *Introduction to Time Series and Forecasting*, Springer, New York, 2002.
11. G. Molnár, A. Gravouil, 2D and 3D Abaqus implementation of a robust staggered phase-field solution for modeling brittle fracture, *Finite Elements in Analysis and Design*, **130**: 27–38, 2017, doi: 10.1016/j.finel.2017.03.002.
12. N. Singh, C.V. Verhoosel, R. De Borst, E.H. Van Brummelen, A fracture-controlled path-following technique for phase-field modeling of brittle fracture, *Finite Elements in Analysis and Design*, **113**: 14–29, 2016, doi: 10.1016/j.finel.2015.12.005.
13. M.N. Dinh, C.T. Vo, C.T. Nguyen, N.M. La, Phase-Field modelling of brittle fracture using time-series forecasting, [in:] *Proceedings of the Computational Science–ICCS 2022: 22nd International Conference*, London, UK, June 21–23, Part II, pp. 266–274, 2022, doi: 10.1007/978-3-031-08754-7_36.
14. J.D. Hamilton, *Time Series Analysis*, Princeton University Press, 2020.

Received June 30, 2024; revised version October 11, 2024;
accepted November 5, 2024; published online December 6, 2024.